RSC Advances

PAPER

View Article Online
View Journal | View Issue

Cite this: *RSC Adv.*, 2022, **12**, 23527

Non-doped and transition metal-doped CuO nanopowders: structure-physical properties and anti-adhesion activity relationship

N. Khlifi,[ac] S. Mnif,[b] F. Ben Nasr,[a] N. Fourati,[c] C. Zerrouki,[c] M. M. Chehimi,[d] H. Guermazi, *[a] S. Aifa[b] and S. Guermazi[a]

Bacterial contamination and biofilm formation generate severe problems in many fields. Among these biofilm-forming bacteria, *Staphylococcus epidermidis* (*S. epidermidis*) has emerged as a major cause of nosocomial infection (NI). However, with the dramatic rise in resistance toward conventional antibiotics, there is a pressing need for developing effective anti-biofilms. So, fabrication of copper oxide nanoparticles (NPs) is one of the new strategies to combat biofilms. Notably, doped CuO NPs in anti-biofilm therapy have become a hot spot of attention in recent years due to their physicochemical properties. In this context, the present work deals with the investigation of undoped and transition metal (TM)-doped CuO NPs (TM = Zn, Ni, Mn, Fe and Co), synthesized *via* the co-precipitation method. The synthesized CuO NPs are characterized using X-ray diffraction (XRD), Fourier transform infrared (FTIR) spectroscopy, field-emission scanning electron microscopy (FE-SEM), energy dispersive spectroscopy (EDS) and X-ray photoelectron spectroscopy (XPS). Results consistently revealed the successful formation of CuO NPs using the co-precipitation method and confirmed that TM ions are successfully inserted into CuO crystal lattice. We found that doping changes the morphology of the CuO NPs and increases their crystallite size. The XPS results show a non-uniform distribution of the doping concentration, with a depletion or an enrichment of the NP surface depending on the element considered. Furthermore, the anti-adhesive potential of CuO NPs against *S. epidermidis S61* biofilm formation is evaluated in this study by crystal violet and fluorescence microscopy assays. All synthesized NPs exhibit considerable anti-adhesive activity against *S. epidermidis S61* biofilm. Interestingly, compared to undoped CuO, Fe and Ni-doped oxides show an improved activity when used at high concentrations, whereas Mn-doped CuO is the most efficient at low concentrations. This makes TM-doped CuO a promising candidate to be used in biomedical applications.

Received 15th April 2022
Accepted 31st July 2022

DOI: 10.1039/d2ra02433k

rsc.li/rsc-advances

1. Introduction

Nanotechnology is an interdisciplinary field that is based on fundamental sciences such as physics, chemistry, and biology and is growing with current developments. Particularly, metal oxide nanoparticles (MONPs) possess special physical and chemical properties due to their finite size and large surface area. These properties make metal oxides an interesting project for scientists because of their multidisciplinary applications.[1–3] Particularly, copper oxide nanoparticles (CuO NPs) have been widely studied and are receiving more attention from many scientists and engineers thanks to their motivating properties and high potential applications in various fields.[4–6] In the energy domain for example, CuO NPs have been considered as electrode materials for the next-generation rechargeable lithium-ion batteries, owing to their abundance, environmental compatibility and eco-friendliness, high theoretical capacity, and non-toxicity.[7] Moreover, both morphology and size remarkably affected their physical properties. As a p-type semiconductor of narrow band gap in visible region, CuO NPs are expected to be good candidate for high potential applications as solar cells, storage devices, and sensors, as well as super capacitors and especially it acts as a good catalyst in some of the chemical reactions.[8–10] In fact, several researchers have been directed towards the photo-catalytic activities of CuO NPs, for the degradation of organic pollutants.[11,12] Recently, CuO NPs have been largely prepared for various applications in fields ranging from semi-conductors to biomedical. For the latter, many studies involving CuO NPs have been carried out on anti-bacterial,[13,14] anti-biofilm,[14] anti-cancer,[15] anti-microbial,[16] and anti-fungal[17] aspects. Among these studies, biofilms were explored several

[a]*Laboratory of Materials for Energy and Environment, and Modeling (LMEEM), Faculty of Sciences, University of Sfax, B.P: 1171, 3038, Tunisia. E-mail: hajer.guermazi@gmail.com*

[b]*Laboratory of Molecular and Cellular Screening Processes, Centre of Biotechnology of Sfax, P.O. Box 1177, 3018 Sfax, Tunisia*

[c]*Laboratory of Information and Energy Technology Systems and Applications (SATIE), UMR 8029, CNRS, ENS Paris-Saclay, CNAM, 292 Rue Saint-Martin, 7503 Paris, France*

[d]*Université Paris Cité, CNRS, ITODYS (UMR 7086), 75013 Paris, France*

centuries ago by researching the link between its formation and the persistence of the disease.

Bacterial biofilms are a growing problem as it is a major cause of nosocomial infection (NI) affecting hospitals worldwide and one of the health issues among all societies. Biofilms, derived from microbe colonized on surfaces, cause persistent infections and are an issue of considerable concern to healthcare providers.[18,19] They caused serious problems to society from both health concerns and economical perspectives.[20] One of the most potentially successful strategies may be the use of nano-materials. Nowadays, the use of NPs is considered one of the future challenges that govern the biomedical applications.[21] Among many NPs, the most promised and widely studied is CuO NPs. Numerous researches indicated that CuO had higher anti-biofilm activity against clinically isolated, biofilm forming, multi-drug resistant micro-organisms such as *Escherichia coli*, *Staphylococcus aureus*[22–24] and *Streptococcus mutans*.[25] However, knowledges about the effect of TM doping on CuO's anti-bacterial activities, is still in its juvenile phase. Likewise, doping CuO with various TM has been considered to enhance the physical/chemical properties of the host material CuO without modification of its structure.[26] Indeed, several researches showed that physicochemical properties of CuO NPs can be modified by doping with a suitable element to meet the pre-determined needs. In particular, the effect of doping of CuO NPs by 3d TM such as $Mn^{2+/3+}$, $Co^{2+/3+}$, $Fe^{2+/3+}$, $Ni^{2+/3+}$ and Zn^{2+}, on their electrical, optical, and magnetic properties were largely considered.[27–31] The control of the synthesis process and the understanding of its mechanism allowed elaborating undoped and TM-doped CuO NPs with specific properties, according to the envisaged applications. The use of TM-doped CuO as anti-biofilm agents has recently attracted considerable attention in biomedical fields.[32,33] In addition, the results show benefits in the use of undoped and/or doped CuO NPs that could work synergistically to provide an anti-biofilm effect against various bacterial strains. Among these bacterial strains, *Staphylococcus epidermidis* strain (*S. epidermidis*) is a major nosocomial pathogen with a remarkable ability to persist on indwelling medical devices through biofilm formation. Unfortunately, *S. epidermidis* strains have become the most common cause of nosocomial infections (NIs) and infections on indwelling medical devices, which typically involve biofilms.[34,35] It is one of the major human pathogen cause's mild superficial infections to severe life-threatening invasive infections to the human world resulting in significant disease and mortality.[36,37]

Several works reported on CuO NPs synthesized by physical, chemical, and biological methods such as sol–gel,[38] co-precipitation,[39] solvo-thermal,[40] microwave irradiation,[41] laser ablation,[42] bio-synthesis using *Verbascum thapsus* leaves extract,[43] and biological methods using the cyanobacteria *Phormidium*.[44] Among these various synthesis methods, co-precipitation is of interest since it is considered as an economical and eco-friendly approach. Moreover, using this technique, shape and particle size of NPs can be tuned by varying different parameters such as pH value, precursor's concentrations, and reaction temperature.

A comprehensive study of the already published reports has thrown light on the fact that no work has been done so far to determine the anti-adhesion activities of different TM-doped CuO NPs compared to pure CuO NPs against biofilm forming by *S. epidermidis* bacteria. In the present work, undoped and TM-doped CuO NPs are successfully synthesized *via* the co-precipitation method. The purpose of the current study is to investigate TM doping of CuO on its potential activity as inhibitors of biofilm formation. The anti-biofilm effect of the prepared samples (TM-doped and undoped CuO NPs) will be correlated to physical and structural changes induced by doping.

The incorporation of anti-adhesive MONPs within or on the surface of materials, or by coatings, to prevent microbial adhesion or kill the microorganisms after their attachment to biofilms, represents an important strategy in an increasingly challenging field.[45] Consequently, this study aimed to evaluate the effectiveness of incorporating 3d TM (TM = Mn, Fe, Co, Ni, and Zn) into the physicochemical properties of CuO NPs and assess its anti-biofilm activity effects against *S. epidermidis S61*.

2. Experimental details and materials

2.1. Materials and synthesis

All chemical reagents, doping precursors either chlorides as manganese chloride tetra-hydrate ($MnCl_2 \cdot 4H_2O$), cobalt chloride hexa-hydrate ($CoCl_2 \cdot 6H_2O$), nickel chloride hexa-hydrate ($NiCl_2 \cdot 6H_2O$), zinc chloride ($ZnCl_2$), or sulfates as iron sulfate hepta-hydrate ($FeSO_4 \cdot 7H_2O$), and sodium hydroxide (NaOH), distilled water and ethanol are supplied by Sigma Aldrich (purity >99%) and used without any further purification.

Undoped (CuO) and TM-doped CuO, TM = Fe, Mn, Co, Zn, and Ni (will be noted as CuO:Fe, CuO:Mn, CuO:Co, CuO:Zn and CuO:Ni respectively), are synthesized through co-precipitation method, using copper sulfate pentahydrate [$CuSO4 \cdot 5H_2O$] as primary precursor.

Firstly, aqueous solution (1 M) of copper sulfate is prepared under magnetic stirring. Subsequently, 50 ml of 1 M NaOH solution is added drop-wise to the homogeneously mixed solution every 15 min under constant stirring, and the pH was maintained between ~11 and ~12. Then, the solution is kept at 25 °C for 3 hours under constant stirring, until a blue precipitate is formed. This precipitate is filtered, and then washed several times with distilled water and ethanol to remove any residue. Finally, the precipitate is dried, ground and annealed at 500 °C for 4 hours to obtain a pure CuO phase and enhance the crystalline quality of the synthesized powder.

The TM-doped samples are also prepared by co-precipitation method. To prepare TM-doped CuO NPs, doping precursors are taken respectively and added separately into the ($CuSO_4 \cdot 5H_2O$) solutions. The remaining process is the same as the synthesis of undoped CuO NPs.

The obtained samples with an expected doping rate of 2 mol% are used for further characterization.

2.2. Characterization techniques

The powder X-ray diffraction (XRD) measurements were carried out at room temperature using a D8 Advance Bruker diffractometer with a Lynx eye accelerator using CuKα_1 radiation (λ = 1.5406 Å) at 40 kV and 40 mA. The angular range 2θ is between

5° and 70° with a step of 0.02°, and a scan rate of 1 step per second. Morphology analysis is undergone using scanning electron microscope (SEM, HITACHIS-3400 N, Japan) at 20 kV. The elemental composition of the samples is analyzed using energy dispersive spectroscopy (EDS) analysis. The chemical signature (molecular vibration energies) of the samples is provided *via* Fourier transform infrared (FTIR) experiments, investigated with a BRUKER spectrophotometer in the 400–4000 cm^{-1} range. X-ray photoelectron spectra (XPS) were acquired using a K Alpha+ machine (Thermo, East Grinsted, UK) fitted with monochromatic Al K alpha source ($h\nu = 1486.6$ eV). The pass energy was set to 80 eV for the narrow regions and 200 eV for recording the survey spectra. A flood gun was used during the surface analysis to compensate for static charge build-up. The surface composition was determined using the manufacturer's sensitivity factors.

2.3. Anti-biofilm activity

The anti-biofilm activities of TM-doped and undoped CuO NPs are performed against *S. epidermidis S61*, a biofilm forming strain in our Laboratory collection.[46] Anti-adherence activities are tested in 96-well flat bottom microtiter plates as described by Nostro *et al.*[47] with some modifications. Nanoparticle solutions (CuO, CuO:Fe, CuO:Mn, CuO:Co, CuO:Zn and CuO:Ni), dissolved in Tryptone Soy Broth (TSB),are subjected to an ultrasonic bath for 1 h at 25 °C. Solutions (100 μl) are then added into the first column of plates and used to perform a serial two-fold dilution. This is followed by the addition of 50 μl of glucose at a final concentration of 2.25% in each well. An overnight culture of *S. epidermidis S61* is performed in TSB medium at 30 °C and diluted with TSB. 50 μL of bacterial suspension are served to inoculate all wells in order to reach a final optical density (OD) of 0.1 at a wavelength of 600 nm. Cell culture without NPs is served as a control. Following incubation for 24 h at 30 °C, TSB and plank tonic cells are discarded by reversing the plate and all wells are washed twice with 200 μL of sterile phosphate buffer saline (PBS) (pH 7.2). The plate is then dried at 60 °C for 1 h. Each well is stained with 150 μL of crystal violet 0.2% (w/v of ethanol 20%) for 15 min. The wells contents are removed and the remaining of crystal violet, which stained the attached bacteria, is rinsed thrice with water. A volume of 200 μL of glacial acetic acid (33% (v/v)) is added in all wells and the solubilisation of biofilm is obtained following the incubation for 1 h at room temperature. Finally, the optical density is measured with the micro-plate reader at a wavelength of 570 nm. Percentage of biofilm inhibition is calculated by the comparison between the absorbance of untreated and treated biofilms according to the following formula:

$$\%\ \text{biofilm inhibition} = \frac{(\text{OD(growth control)} - \text{OD (sample)})}{\text{OD(growth control)}} \times 100 \quad (1)$$

The effect of TM-doped CuO NPs on biofilm inhibition is confirmed by the fluorescence microscopy. To visualize the biofilm inhibition, cultures of *S. epidermidis* (in TSB plus 2.25% glucose) are grown on round cover slips (diameter 1 cm) immersed in a 24-well polystyrene plate with or without (control) NPs addition. Incubation of plates for 24 h at 30 °C, is followed by removal of the medium and subsequent cover slips washing with sterile PBS (1X, pH 7). The fluorescent dye Acridine orange, at a concentration of 0.1% w/v in PBS 1X, is used to stain the formed biofilm in cover slips during 15 min. Biofilms were imaged with a OLYMPUS fluorescent microscope BX50 equipped with a digital camera OLYMPUS DP70 using an appropriate filter.

All experiments are done in triplicate. The obtained results are expressed as mean values with the standard error. The statistical analyses are performed using Student's *t*-test to compare the controls and treatment conditions at a significance level of 5%.

3. Results and discussion

Discovering the key factors involved in biofilm inhibition will allow exploring the utilization of undoped and TM-doped CuO NPs in biomedical applications. So, it is necessary to determine the relevant physico-chemical parameters such as crystallite size, shape, surface area, composition, and morphology, which could be advantageously, involved in the anti-biofilm activities.

3.1 Structural studies by X-ray diffraction (XRD)

XRD patterns of the undoped and TM-doped CuO NPs are shown in Fig. 1. The diffraction peaks in all samples matched well with the typical CuO monoclinic structure with *C*2/*c* symmetry according to the International Center for Diffraction Data (ICDD card no. 01-089-2529)[48] and were assigned to the (110), (002), (111), (−202), (020), (202), (−113), (−311) and (113) planes. Besides the absence of significant change in the crystal structure, no secondary oxide phases are detected in samples, indicating pure CuO phase formation, and the successful insertion of the doping elements in CuO lattice during the growth process. However, micro-changes undoubtedly occur in terms of characteristic parameters and/or in terms of micro-strain, and therefore need to be analyzed more closely. Lattice constants (a, b, c, and β) of the monoclinic structure and unit cell volume (V) of prepared samples are estimated from the diffraction peaks, using the following equations:[49]

$$2d_{hkl}\sin\theta = n\lambda \quad (2)$$

$$\frac{1}{{d_{hkl}}^2} = \frac{1}{\sin^2\beta}\left(\frac{h^2}{a^2} + \frac{k^2\sin^2\beta}{b^2} + \frac{l^2}{c^2} - \frac{2hl\cos\beta}{ac}\right) \quad (3)$$

$$V = abc\sin\beta \quad (4)$$

where θ is the Bragg's diffraction angle, λ is the wavelength of the used Cu Kα radiation, d_{hkl} is the (hkl) interplanar spacing.

The obtained values of lattice parameters for the synthesized NPs are gathered in Table 1. As expected, we notice some changes of crystal lattice parameters, in consequence of doping with transition metals.

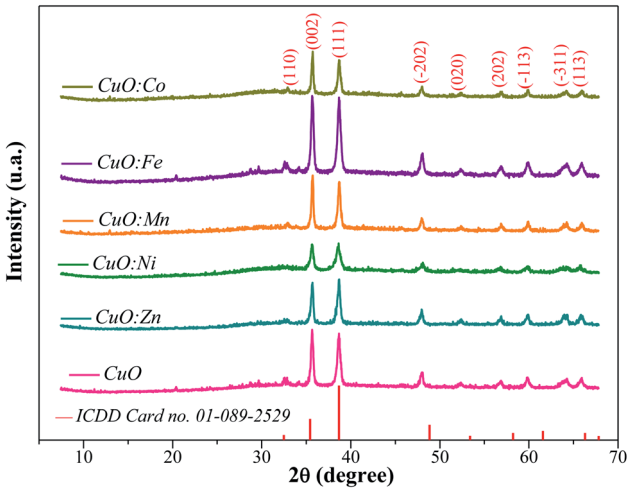

Fig. 1 XRD patterns of CuO, CuO:Fe, CuO:Mn, CuO:Co, CuO:Zn and CuO:Ni samples.

Table 1 Structural parameters of undoped and M-doped CuO NPs

Synthesized NPs	Lattice parameters				
	a (Å)	b (Å)	c (Å)	β (°)	V (Å^3)
CuO	4.863	3.433	5.136	99.309	84.638
CuO:Fe	4.881	3.427	5.138	99.455	84.776
CuO:Zn	4.791	3.430	5.137	99.546	83.291
CuO:Mn	4.700	3.432	5.133	99.549	81.660
CuO:Co	4.701	3.431	5.131	99.470	81.656
CuO:Ni	4.644	3.454	5.136	99.309	81.327

The unit cell volume of CuO NPs is sensitive to TM doping, as shown by the values gathered in Table 1. A reduction between 1.6 and 3.9% is observed depending on the elements considered, except for Fe for which we notice a very slight increase (of 0.2%).

The relative differences between the ionic radii, extracted from the reference database (Ni^{2+}: 0.69 Å, Mn^{2+}: 0.67 Å, Co^{2+}: 0.65 Å, Cu^{2+}: 0.73 Å, Zn^{2+}: 0. 74 Å and Fe^{2+}: 0.78 Å),[50] do not allow correlating the effects of the dopants in the volume to their ionic radius alone, as one could be tempted to do at first approach. The dispersion of results proves that other intrinsic parameters (electro negativity for example) or experimental ones, act in a correlated way on the properties of the obtained products including their mesh parameters. However, the difference between the synthesized NPs (increase of the unit cell volume in case of iron and decrease for Ni, Zn, Co and Mn), let us expect a sufficient difference in their physical properties and, consequently, in their potential anti-biofilm activities.

To further investigate the effect of doping, we focused on the two most intense Bragg's peaks corresponding to the (002) and (111) plans, which we fitted by a Gaussian model (Fig. 2(a) and (b)).

For the peak (002) (Fig. 2(a)), we observe a slight shift towards the high angles for Fe and Mn doping. For the other elements and given the accuracy of about 0.01°, the observed

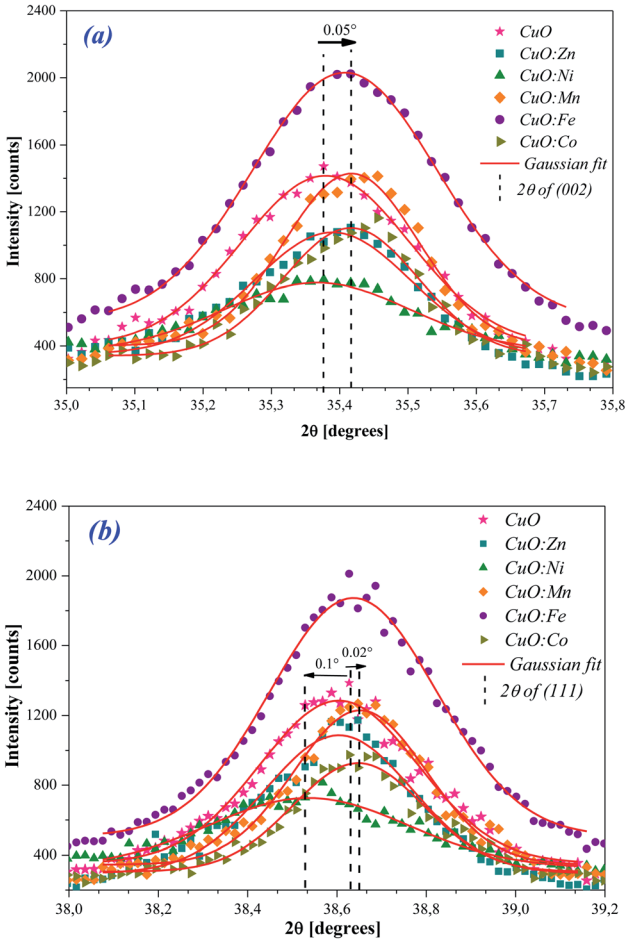

Fig. 2 The Gaussian fit to the (a) (002) and (b) (111) diffraction peaks of undoped and TM-doped CuO NPs.

shift is too small to be judged. For the peak (111) (Fig. 2(b)), we still observe a slight shift towards the high angles for Fe and Mn doping, but also for Co this time. As for the Ni doping, it produces a shift in the opposite direction.

In Fig. 3, we gathered the intensity ratio $I_{(002)}/I_{(111)}$ of the main peaks, for all NPs oxides.

By considering the $I_{(002)}/I_{(111)}$ peak intensity ratio as discriminating parameter (Fig. 3), we notice that this parameter decreases for all doped oxides. Nevertheless, its value remains slightly superior to the unit for all oxides except for CuO:Zn sample. This means that the crystalline growth of undoped and Ni, Mn, Fe and Co-doped CuO NPs occurred preferentially according to the (002) direction while an inversion is observed for the crystallites of CuO:Zn NPs, which preferentially grow in the (111) direction. From these results, we can note that the insertion of transition metals within the CuO matrix induces some structural changes and moderately affects the preferential growth direction.

To complete this comparative structural study, microstructural parameters such as crystallite size (D), specific surface area (SSA), micro-strain (ε) and dislocation density (δ) were investigated for all the synthesized samples.

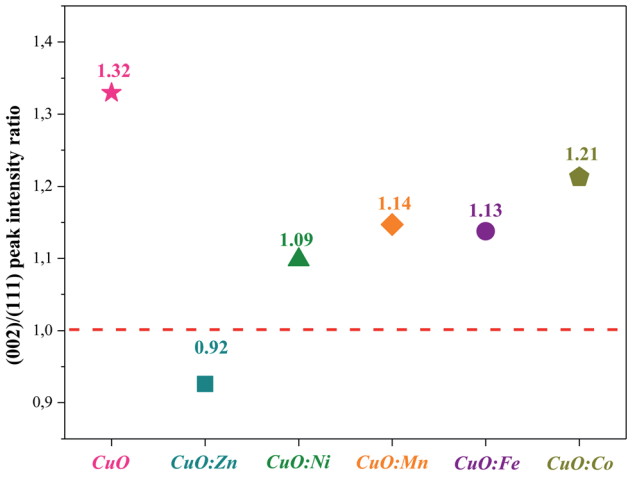

Fig. 3 $I_{(002)}/I_{(111)}$ peak intensity ratio of undoped and TM-doped CuO NPs.

The average crystallite size and lattice strain were deduced from the broadening of the XRD peak by the relation:[51]

$$\beta^2_{(hkl)} = \beta^2_{\text{size}} + \beta^2_{\text{strain}} \quad (5)$$

where β_{size} and β_{strain} are the broadening contributions due to crystallite size and strain, respectively.

Afterward, Debye–Scherrer (D–S) method[52–55] is used to estimate the average crystallite size from the equation:

$$D = \frac{k\lambda}{\beta_{\text{size}}\cos\theta} \quad (6)$$

where λ is the wavelength of X-ray radiation (1.5406 Å), $k = 0.9$ is the shape factor, D is the average crystallite size, and θ is the Bragg's diffraction angle.

However, the effect of strain and imperfections on the line broadening differs from the effect of crystalline size. The micro-strain induced in the prepared powders is calculated using eqn (7).

$$\varepsilon = \frac{\beta_{\text{strain}}}{4\ \tan\theta} \quad (7)$$

Moreover, the dislocation density (δ) of the crystal is evaluated using the following formula:[56]

$$\delta = \frac{1}{D^2} \quad (8)$$

The SSA is intimately linked to particle size, but other parameters, such as the microstructure and morphology of the materials, can greatly affect its value. Particle size determination was considered as an indirect estimate of the SSA values. This extremely important parameter greatly affects the properties of the NPs, and influences their mode of interaction with the surrounding media.

Assuming that the particles have a spherical shape, we can estimate the SSA from the crystallite size determined by Scherrer equation, using formula eqn (6):[57,58]

$$S = \frac{6}{D \times \rho} \quad (9)$$

$$\rho = \frac{n \times M}{N \times V} \quad (10)$$

S is the SSA [$m^2\ g^{-1}$], ρ is the density of the particles [$g\ cm^{-3}$], M is the molar weight of substance ($M_{CuO} = 79.545\ g\ mol^{-1}$), n is the number of formula units in the unit cell ($n = 4$ for CuO according to the ICDD data no. 01-089-2529), V design the volume of the unit cell (eqn (2)) and N is the Avogadro's number ($N = 6.02214 \times 10^{23}\ mol^{-1}$). The calculated values of SSA and the density (ρ) are added in Table 2.

These values clearly show that the structural parameters exhibit slight variations, as consequence of the incorporation of TM ion within CuO host lattice. Moreover, it is found that the micro-strain decreases with doping compared to the undoped CuO NPs, except for CuO:Fe. An increase in the average crystallite size is thus clearly observed for all TM-doped CuO samples compared to undoped CuO. However, the CuO:Fe shows the smallest crystallite size and the highest micro-strain of the all-doped samples, while the largest crystallite size associated with the lowest micro-strains are obtained with Zn doping.

Fig. 4 depicts the evolution of the SSA of the synthesized NPs as a function of the average crystallite size for undoped CuO and TM-doped oxide with different metal transition elements.

As expected, and inversely to the crystallites size, the highest SSA value of 70 $m^2\ g^{-1}$, has been obtained for the undoped CuO NPs. For all the TM-doped CuO NPs, SSA values are smaller, and the lowest one is associated to CuO:Zn sample (26 $m^2\ g^{-1}$). All estimated SSA values are higher than the typical specific surface

Table 2 Micro structural parameters of undoped and M-doped CuO NPs

Samples	Crystallite size, D (nm)	Micro-strain ε ($\times 10^{-2}$)	Dislocation density, δ ($\times 10^{15}\ m^{-2}$)	Density of the particles ρ ($g\ cm^{-3}$)	Specific surface area, S ($m^2\ g^{-1}$)
CuO	13.712	0.75	5.318	6.242	70.101
CuO:Zn	36.132	0.47	0.765	6.343	26.179
CuO:Ni	22.243	0.57	2.021	6.496	41.525
CuO:Mn	19.043	0.71	2.757	6.470	48.698
CuO:Fe	14.474	0.84	4.773	6.232	66.517
CuO:Co	19.666	0.61	2.585	6.470	47.155

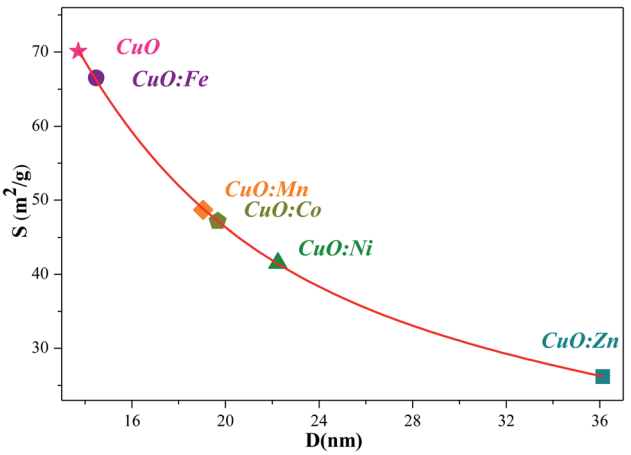

Fig. 4 Relationship between the SSA and the average crystallite size (*D*) of undoped and TM-doped CuO NPs.

area values of high purity commercially available CuO nanopowders (*i.e.* ≥99.99%), in the range of 10 to 15 $m^2\ g^{-1}$ (for example Get Nano Materials, American Research Nano-materials…). Obviously, the estimated SSA values are dependent on several assumptions, mainly a homogenous spherical shape, and are therefore subject to uncertainties. Nevertheless, they remain interesting because they are high despite uncertainties, and they are different one from the other. These are two important reasons which prompt us to test the NPs, we successfully synthesized, against bacterial activity.

It is noted that the specific surface area and surface to volume ratio increase dramatically as the size of materials decreases. The surface states will play an important role in the NPs, due to their large surface to volume ratio with a decrease in particle size.[59] It has a more importance in case of adsorption, heterogeneous catalysis and reactions on surfaces. Also, in biomedical field, NPs are preferred over other agents because of their small size, large surface area and highly reactive nature.[60] Then, the consistence between surface area and crystallite size values estimated from XRD pattern data using Scherer method indicates that both undoped and-doped CuO NPs has surface activities. The reactivity of the NPs varies according to its surface function, particle size, shape, and state of aggregation.[61]

Hence, exact knowledge around the surface chemistry of NPs is important before their applications. Fourier transform infrared (FTIR) technique can be effectively used to gain information about the surface chemistry of our samples.

3.2. Fourier transform infrared (FTIR) study

The Fourier transform infrared spectroscopy (FTIR) is carried out to identify the main chemical bonds in the synthesized CuO samples. Fig. 5(a) and (b) shows the FTIR spectra of prepared samples in the range (400–4000 cm^{-1}). However, for better clarity of region of interest, FTIR spectra are enlarged in a selective range of 400–1300 cm^{-1} (Fig. 5(b)). In the range of 400–700 cm^{-1} (Fig. 5(a) and (b)) IR spectra display vibrational bands ascribed to stretching mode of CuO bonds.[62–65] In addition, a broad band in the region 3200–3600 cm^{-1} (Fig. 5(a)) can

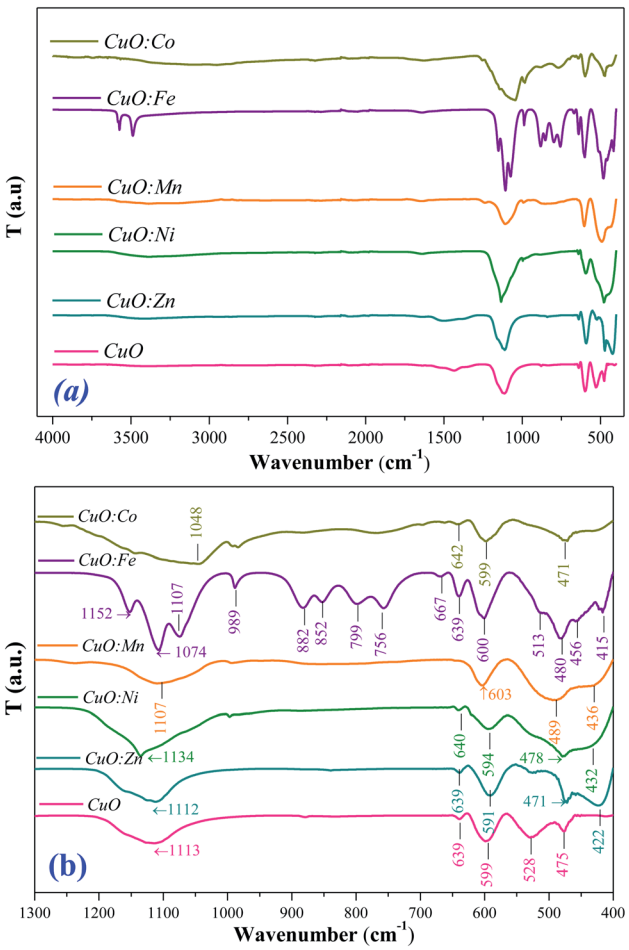

Fig. 5 FTIR spectra of CuO and TM-doped CuO NPs (a) in 400–4000 cm^{-1} range, and (b) enlarged spectra from 400 cm^{-1} to 1300 cm^{-1}.

be attributed to the stretching vibration of the O–H bonds,[66–69] due to adsorbed water molecules on the CuO NPs surface. Moreover, all samples have the absorption bands in the 1434–1643 cm^{-1} range that may be assigned to O–H bending vibrations, combined with copper atoms.[70] As shown in FTIR spectra (Fig. 5(b)), new bands appear between 750 cm^{-1} and 990 cm^{-1}, which can be attributed to degenerate and non-degenerate modes of SO_4 groups respectively.[71] In this way, the broad band around 1112 cm^{-1} is the evidence of the existence of SO_4^{2-} in the all analyzed samples.[72–74] Indeed, the precursors of copper is the sulfate type ($CuSO_4 \cdot 5H_2O$).

No other active modes corresponding to other species like Cu_2O or Cu $(OH)_2$ or other peaks from doping elements were detected, agreeing with the XRD analysis which confirms the purity of prepared samples. In addition, no bands related to TM–O vibrations have observed, which confirms the successful substitution of doping ions in CuO structure, and the purity of CuO phase. All observed bands are found to be shifted towards higher wave-number side for all doped CuO NPs. This shift can be due to the perturbation of CuO bonding and the difference in the bond lengths as a result of the incorporation of doping ions

in the CuO host lattice.[62–65] Indeed, TM-doping can induce strong interactions between the 3d TM ions and the CuO network. Also, it can originate from size induced lattice variations and crystal defects such as the surface unsaturated coordination sites and edge dislocations induced by doping elements.[75]

3.3. Scanning electron microscope (SEM) and energy dispersive spectroscopy (EDS) analysis

The surface morphology and elemental composition of the synthesized samples are investigated using SEM – EDS analysis.

The SEM images of undoped and TM-doped CuO NPs are shown in Fig. 6(a)–(f). It is noted high agglomerated particles. The observed agglomeration is mainly due to the OH groups (as shown in FTIR spectra) present at the surface of NPs. It is obvious that doping cause morphological changes of grains that affect their SSA (Fig. 4). The variation in the shape and size of NPs is, in fact, the consequence of added doping element in reactional mixture. It may be due to weak inter-intra particle forces. This can influence the potential of anti-biofilm activity of the CuO NPs.

EDS analysis is performed at different locations on each sample, to examine its purity and elemental chemical composition. From the EDS spectra, variation of the intensity [cps/eV] as a function of the energy [keV] (Fig. 7), we identify the chemical elements present in the synthesized samples. The intense peak, located at 0.99 keV, is assigned to the L peak of Cu.[76] Oxygen characteristic peak is present at 0.520 keV.[76] Carbon (C) is detected around 0.270 keV, it originates from the substrate. Thus, the EDS spectra show only the elements copper (Cu), oxygen (O) and TM doping elements (= Zn, Ni, Mn, Fe and Co) and no other elements were observed for

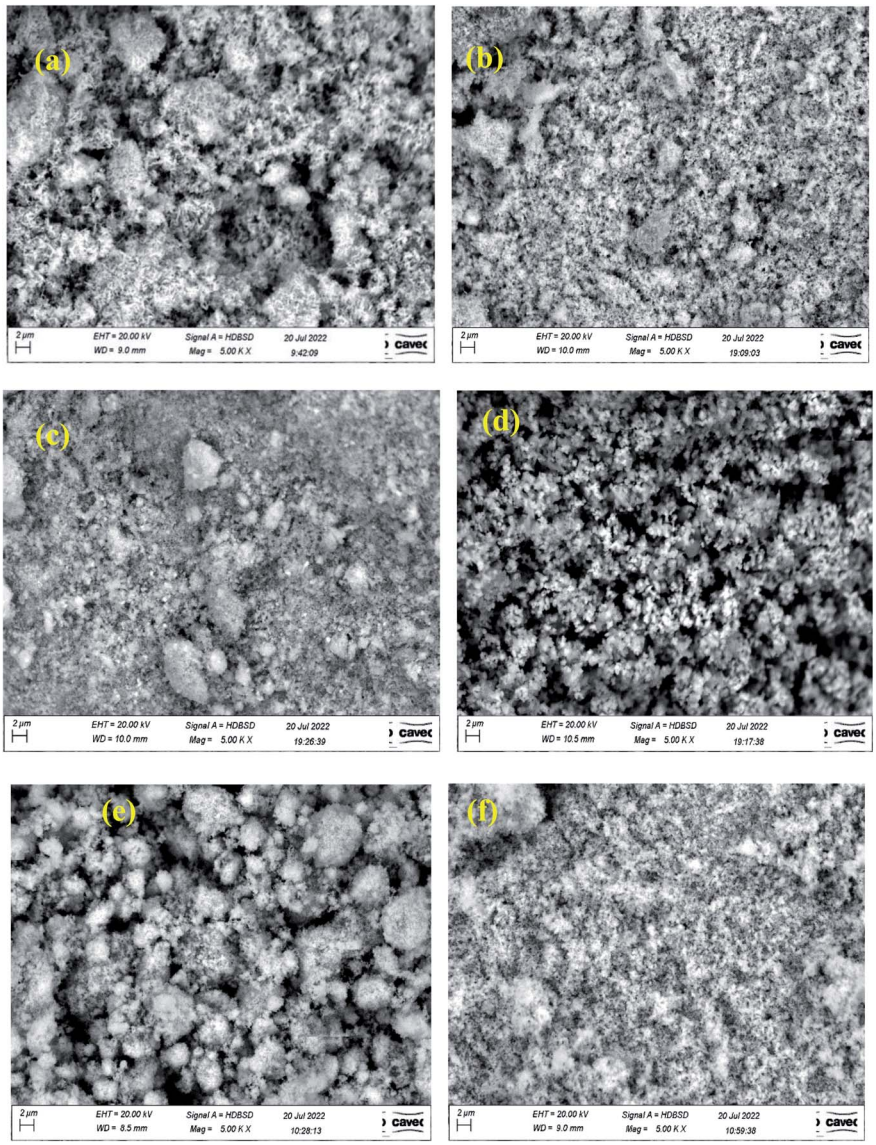

Fig. 6 High magnification SEM images of (a) undoped CuO, (b) CuO:Zn, (c) CuO:Ni, (d) CuO:Co, (e) CuO:Fe, and (f) CuO:Mn.

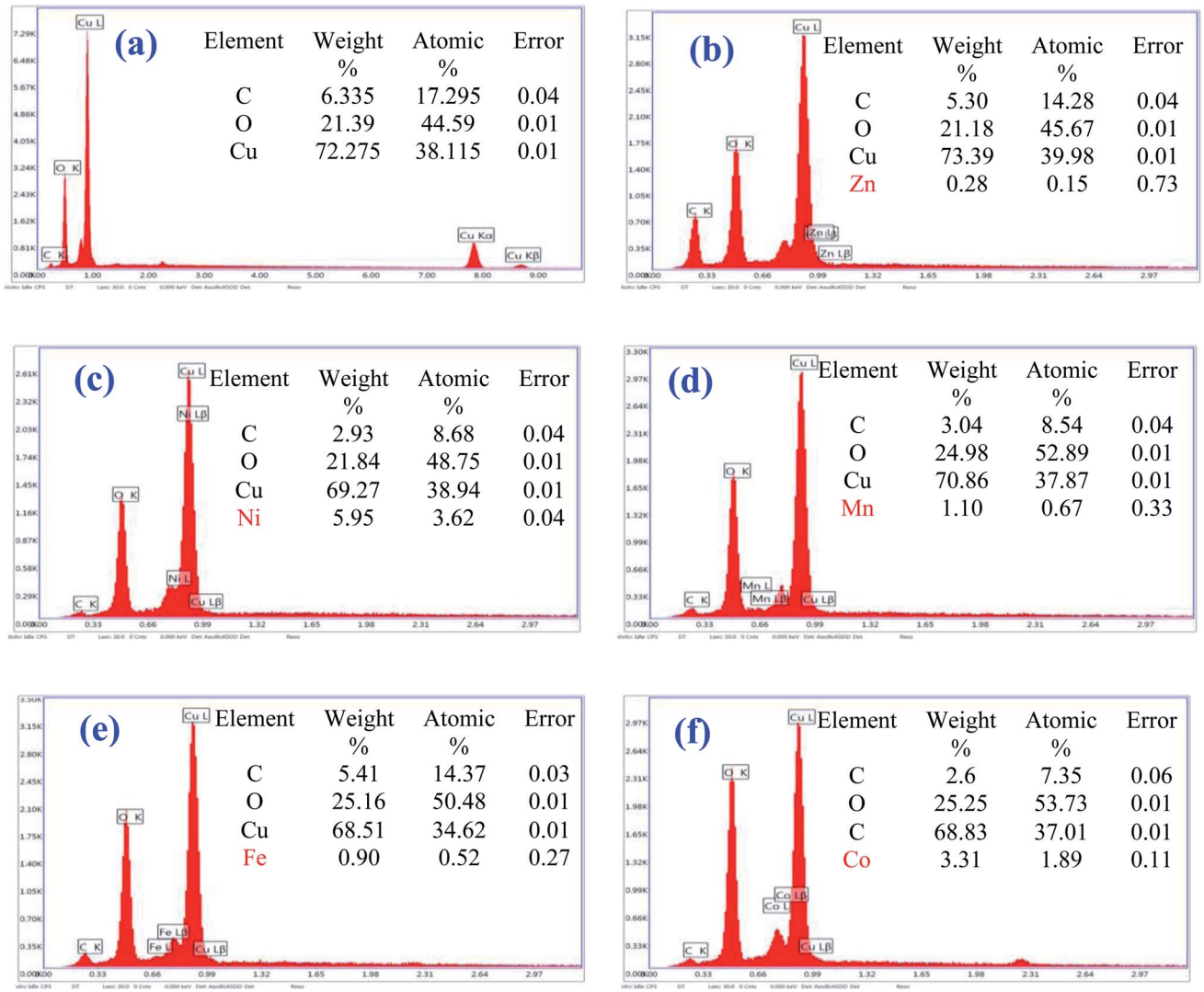

Fig. 7 EDX spectra of (a) undoped CuO, (b) CuO:Zn, (c) CuO:Ni, (d) CuO:Mn, (e) CuO:Fe, and (f) CuO:Co NPs.

undoped and TM-doped copper oxide NPs. So, undoped CuO sample contains characteristic peaks of Cu (K_α, K_β and L_α), O (k_α) and C (K_α) and no significant impurities (Fig. 7(a)). Whereas TM-doped CuO NPs spectra show a signature (L_α and L_β) of each doping element, besides those of Cu (L_α and L_β), and O (k_α) (Fig. 7(b–f)). The presence of the Carbon (C) in the spectra of all samples is due to the substrate based on conductive carbon glue, used as a support during the analysis.

The quantitative analysis obtained from the EDS experiment must be considered with caution because the spectra are convolved, and the deconvolution is even more precise as the gap between the fluorescence lines is high (compared to the resolution of the detector).

For Mn and Fe, whose characteristic lines are relatively separated from those of Cu, 290 eV and 220 eV respectively, the doping rates are estimated at 1.8% and 1.5% respectively. These rates are relatively close to the expected 2%, in contrast with those of Ni (9%) and Zn (0.4%) whose characteristic lines are only 80 eV from Cu (by default for Ni and by excess for Zn). In the case of Co, the doping rate is estimated at 5%. This value is two and a half times higher than expected and shows that the doping technique is not yet fully mastered. Of course, this point deserves to be further elucidated in the future, to control the doping rate on the one hand and to quantify it with precision on the other. But at this stage what is important is to have succeeded in doping with all the elements considered, allowing considering the biological tests in a comparative way with the non-doped CuO. Nevertheless, we have considered XPS analyses to confirm in a complementary way the presence of dopant atoms within the CuO matrix.

3.4. Surface chemical analysis by XPS

X-ray photoelectron spectroscopy (XPS) was used to examine the chemical state of the host and doping elements in samples. The XPS survey and narrow regions are displayed in Fig. 8. For the sake of clarity, survey regions are displayed for CuO (Fig. 8a) and CuO:Zn (Fig. 8b) only. Indeed, all other doped CuO particles did not show any striking differences in the

survey regions; all other survey spectra resemble that of pure CuO. Cu2p in the 930–965 eV range is clearly visible together with the prominent Auger peaks. O1s is centred at 529–530 eV, and C1s from adventitious hydrocarbon contamination is placed at ~285 eV. The survey region from CuO:Zn exhibits clearly the Zn 2p doublet. No such clear appearance on the survey scan was noted for Mn, Fe, Co and Ni dopants. These elements could be probed only after acquisition of their

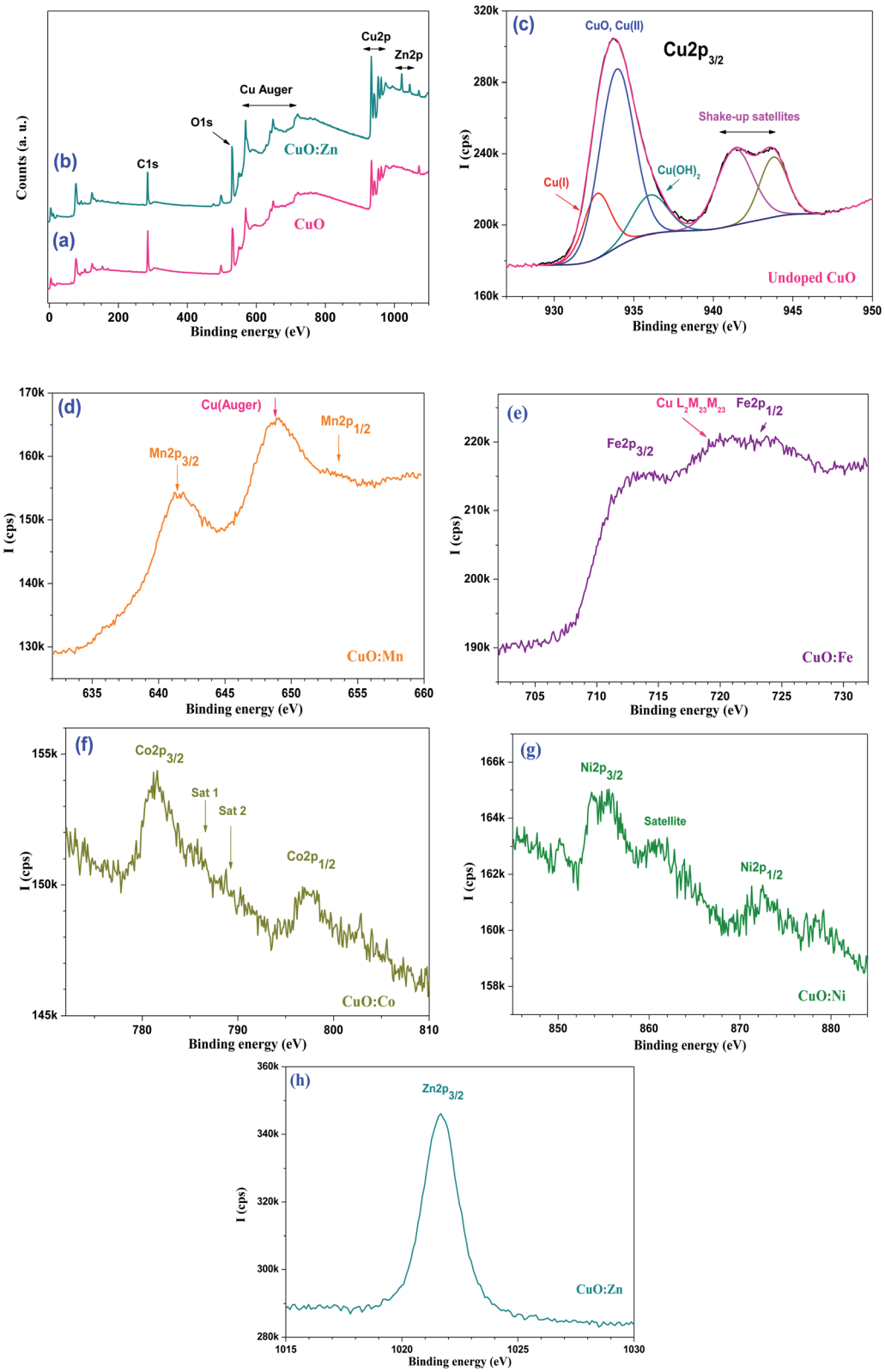

Fig. 8 Survey regions from (a) CuO and (b) CuO:Zn; as well as high resolution spectra of (c) Cu 2p from undoped CuO, (d) Mn 2p from CuO:Mn, (e) Fe 2p from CuO:Fe, (f) Co 2p from CuO:Co, (g) Ni 2p from CuO:Ni, and (h) Zn $2p_{3/2}$ from CuO:Zn.

Table 3 Comparison of dopant to copper atomic ratio determined by XPS and EDS

Technique	Mn/Cu	Fe/Cu	Co/Cu	Ni/Cu	Zn/Cu
XPS	0.33	0.25	0.057	0.038	0.12
EDS	0.018	0.015	0.051	0.093	0.004

corresponding main 2p core level spectra. Fig. 8c displays the peak fitted Cu $2p_{3/2}$ region from pure CuO. There is one prominent peak at ~934 eV and its satellite doublet with two peaks at 941.3 and 943.8 eV, assigned to the so-called shake-up satellites. This is the mark of Cu(II) chemical state. The first main peak is fitted with three components centred at 932.7 (Cu(I), 933.9, and 936 eV, assigned to Cu(I), Cu(II) from CuO, and possibly $Cu(OH)_2$, respectively. It is to note that the *in situ* reduction of Cu(II) is very likely to occur in XPS, and this noted even if the whole set of recording of the core level peaks starts with copper. The difference between the peak position of Cu(I) and Cu(II) is in line with the literature.[77] All other Cu 2p peaks from the CuO:M series look the same, for the simple reason that doping at such low level does not alter the spectral shape of Cu 2p from the major CuO material. Mn 2p, Fe 2p, Co 2p, Ni 2p and Zn $2p_{3/2}$ spectra are displayed in Fig. 8((d)–(h). The Mn 2p doublet (Fig. 8(d) displays two peaks at 641.2 and 653.5 eV, assigned to Mn $2p_{3/2}$ and Mn $2p_{1/2}$, respectively. It is difficult to further exploit the Mn 2p doublet for quantification as it is convoluted with a strong Auger peak from copper. Nevertheless, the Mn 2p region could possibly be assigned to oxidized manganese in the form of Mn_3O_4.[78]

Fig. 8(e) shows the Fe 2p region, another one which is convoluted with Cu $L_3M_{23}M_{23}$ Auger transition.[79] Fe $2p_{3/2}$ is located at ~713.0 eV, and could be assigned to Fe_2O_3. This is confirmed by the occurrence of Fe $2p_{1/2}$ positioned at ~724.2 eV.[80]

Fig. 8(f) displays the Co 2p doublet from CuO:Co with Co $2p_{3/2}$ and Co $2p_{1/2}$ centred at 781.5 and 797.4 eV, respectively. These values are in line with $Co(OH)_2$.[81] The binding energy position of Co $2p_{3/2}$ is not in line with neither Co_3O_4, nor CoO.[78] One can also note the presence of satellites reported for $Co(OH)_2$ in line with those reported in the literature (satellites Sat 1 and Sat 2 at 786.2 and 790.2 eV, respectively).[82]

Ni 2p doublet is shown in Fig. 8(g); Ni $2p_{3/2}$ is centered at ~855.0 eV, whilst the Ni $2p_{3/2}$ satellite is located at 860.8 eV, both peak positions are consistent with nickel(II) oxides/hydroxides $NiO/Ni(OH)_2$.[78]

Fig. 8(h) shows the Zn $2p_{3/2}$ peak from CuO:Zn, centered at 1021.7 eV. It is well known from the XPS literature that it is difficult to use Zn 2p core electron level to distinguish Zn from ZnO. For this reason, we have recorded the Zn Auger peak ($L_3M_{45}M_{45}$) and determined α, the Zn Auger parameter (α = BE (Zn $2p_{3/2}$) + KE (Zn Auger); KE = kinetic energy of the Auger electron). Herein, α = 2010.8 eV and fits in with ZnO of which α values are reported to be in the 2009.5–2011 eV range.[78]

The Auger parameter obtained in this work is much lower than that of metallic zinc (2013.4–2014.4 eV) implying that zinc is in the oxidized state.

We have determined the transition metal (TM) dopant to copper atomic ratio (TM/Cu) and compared to the same ratios determined by EDS (Table 3).

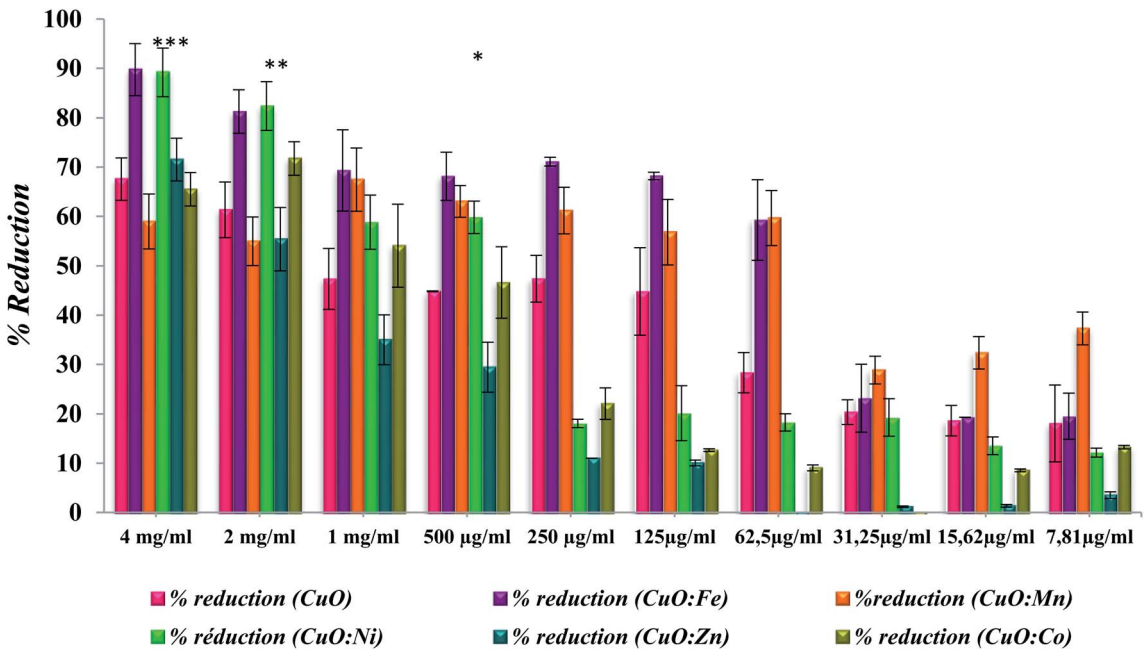

Fig. 9 Anti-adhesive activity of doped and un-doped CuO NPs applied at different concentrations expressed as biofilm inhibition. The results are presented as means ± SD of three independent experiments. *$p < 0.05$, **$p < 0.01$ or ***$p < 0.001$ *versus* control values (undoped CuO) and only significant improvements are presented.

With the exception of cobalt for which the Co/Cu atomic ratio determined by XPS is matching that obtained by EDS, all other ratios indicate gradient distribution of the dopant. Zinc is most likely to be depleted to the surface as the XPS determined Zn/Cu ratio (surface) is higher than that of the obtained by EDS (bulk). Nickel shows 3-fold lower surface Ni/Cu ratio, indicating depletion from the surface and preferential existence of copper at the surface. For Mn and Fe, obviously the ratios are over-estimated as the core electron peaks Mn 2p and Fe 2p are convoluted with Auger lines from copper. Nevertheless, these values indicate depletion in volume of these two elements, probably due to diffusion to the surface.

As far as interactions are concerned, XPS is an ideal technique for probing interactions *via* electron transfer. However, all values reported for CuO and their dopants fall within the binding energy ranges reported for the probed transition metal compounds. Attempts to relate the trends to the electro-negativity of oxidized transition metals M^{2+} are not successful due to very close values of electro-negativity: Mn^{2+} (1.303) < Fe^{2+} (1.341) < Co^{2+} (1.349) < Ni^{2+} (1.367) < Cu^{2+} (1.372) > Zn^{2+} (1.336).[83]

3.5. Anti-biofilm activities of undoped and doped CuO NPs

Anti-adherence activity using crystal violet quantification method is summarized in the following graph (Fig. 9). All doped and undoped CuO NPs show significant anti-adhesive activities on the tested concentrations from 7.81 μg ml^{-1} to 4 mg ml^{-1}. Generally, the activity is dose dependent. The activity is significantly improved with NPs-doped with Fe and Ni at high concentrations in comparison with undoped CuO at the same concentrations. In fact, at 4 mg ml^{-1} of CuO:Fe the activity is significantly improved from 67.56% (for undoped) to 89.75% (CuO:Fe), and the *p*-value is <0.001. The activity is significantly improved also with Ni at concentrations of 2 and 4 mg ml^{-1} with *p*-value of 0.008 and 0.009, respectively (Fig. 9). The activity is not significantly improved with Mn doping at low concentrations from 7.81 to 31.25 μg ml^{-1} (*p*-value> 0.05). Doping with Zn and Co seems to be inefficient which is not in agreement with previous studies showing the effect of doping with Zn in improvement of antibacterial activity against *Streptococcus mutants*.[25] In previous studies, Pugazhendhi *et al.*[33] showed that CuO:Fe could inhibit *S. epidermidis* biofilm formation of approximately 88% which is slightly in agreement with our study in which the inhibition of biofilm formation is close to 70% using CuO:Fe at 125 μg ml^{-1}.

All the tested oxides showed activity, of which the importance depends on the nature of the doping element. This is probably due to their high capacity of absorbing oxygen, giving them a semi-conducting p-type behavior. Excess oxygen increases NPs bacterial activity. The doping of TM into the CuO structure causes distortion, lattice strain, and defect generation in the base structure, as well as ROS generation, leading to the anti-biofilm activity of NPs.

To highlight the benefit of CuO doping, results are expressed in terms of the enhancement of the anti-adhesive activity of some TM-doped CuO NPs, compared to that of undoped CuO (Fig. 10(a) and (b)). For concentrations below 25 μg ml^{-1}, Mn doping leads to an increase in adhesion inhibition efficiency of more than 30% compared to undoped CuO. This improvement even exceeds 75% for the lowest concentrations (lower than 16 μg ml^{-1}). An improvement is also observed in the case of Fe doping with an increase exceeding 40% for concentrations above 100 μg ml^{-1} (Fig. 10(a)). For the highest concentrations, between 500 μg ml^{-1} and 4 mg ml^{-1}, the improvements compared to undoped CuO are brought by Fe and Ni doping. In the case of Fe, the efficiency increase is between 32 and 52%, while for Ni it is about 30% on average (Fig. 10(b)).

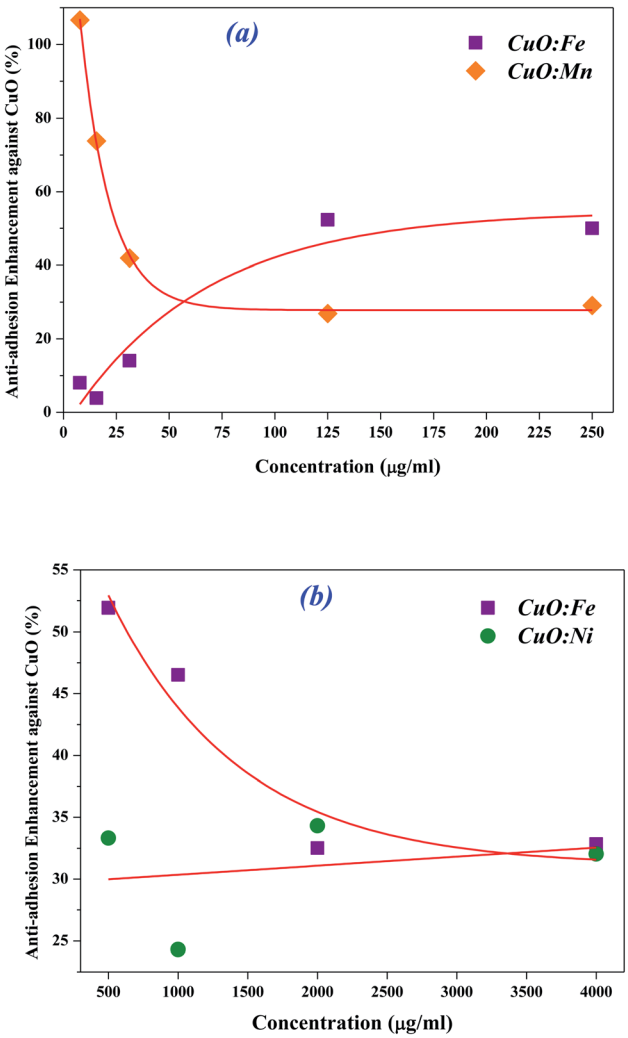

Fig. 10 Enhancement rate of anti-adhesive activity of NPs-doped with (a) Fe and Mn at lower concentrations and (b) Fe and Ni at higher concentrations, in comparison with undoped CuO.

This suggests that the efficiency could be further improved, considering not only one type of doped NPs but a mixture of them. By combining low concentration CuO:Mn NPs with high concentration CuO:Fe NPs, we could achieve a better inhibition of biofilm adhesion. This will be investigated in our future work.

3.6. Biofilm imaging after treatment with doped CuO NPs

Fluorescent microscopy was used to confirm the anti-adherence activity of doped or undoped CuO NPs. Images obtained for

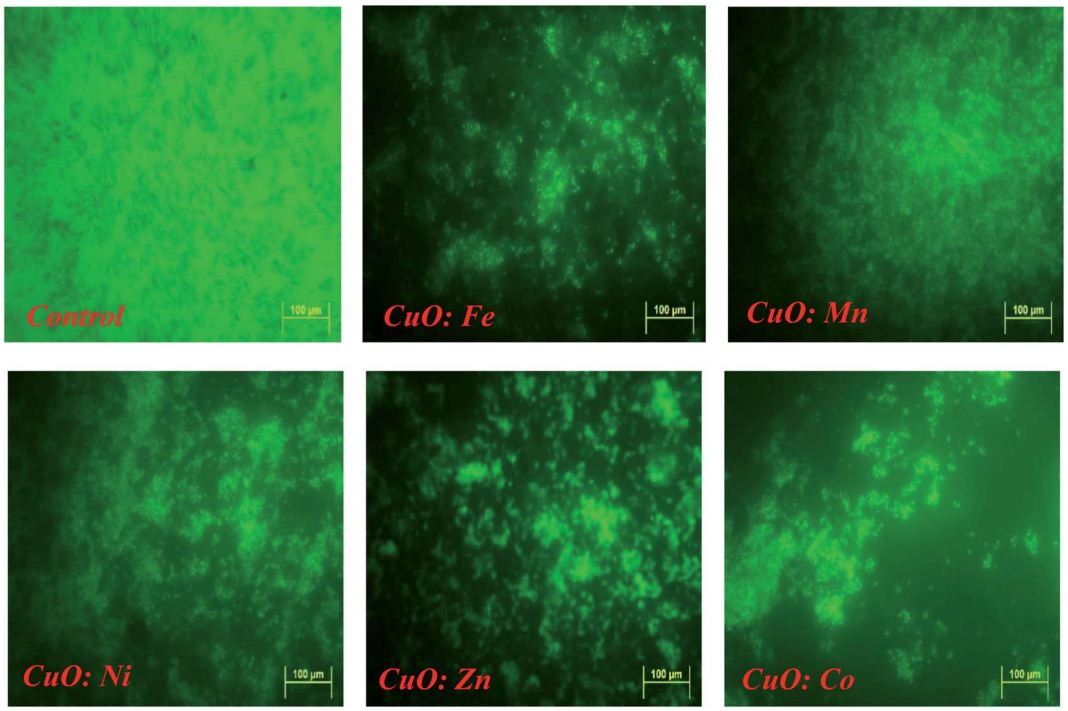

Fig. 11 Fluorescence microscopy with biofilm cover slips. Biofilms were stained with acridine orange. Bar equals 100 µm. Images obtained with control (untreated biofilm) and treated biofilm with doped NPs (at 400 µg ml^{-1}) are presented.

untreated control and doped CuO NPs confirmed the activity, obtained after crystal violet quantification, as showed in the following figure (Fig. 11).

All treatments resulted in a significant reduction in biofilm adhesion, confirming the NPs anti-adhesive activity, already assessed by crystal violet analysis. Anti-adhesion properties of MONPs against biofilm formation are not fully understood. Researchers proposed multiple mechanisms for the damage caused by CuO NPs to bacteria.

3.7. The mechanism of interaction CuO NPs – bacteria in biofilms

Researchers have demonstrated that the mechanism of interaction between NPs and bacteria depends on several factors (*e.g.* physic-chemical properties of NPs).[54,84,85] In fact, the toxicity strength of MONPs depends on the natural toxic properties of heavy metals. It seems that there is a quantitative relationship between average size, surface area and the concentration of MONPs, as described in the last discussions. It is well known that the mechanisms of oxide NPs toxicity against biofilm bacteria are complex and depend on several factors such as composition, surface modification, intrinsic properties (average size, surface area, …), and the bacterial species (Gram-positive or Gram-negative bacteria). A simplified mechanism is proposed in this paper.

Several studies report that the nanotoxicity of NPs is generally triggered by the induction of oxidative stress by free radical formation, following the administration of NPs.[86,87] The mechanisms underlying the anti-adhesion and antibacterial effects of NPs are not completely understood and vary from the productions of oxidative and/or free radical formation (*e.g.*, reactive oxygen species; ROS) stressors to bacteria damage. ROS are ions or small molecules that contain free radicals ($^{\bullet}OH$), peroxide (*e.g.*, hydrogen peroxide; H_2O_2), or oxygen ions (*e.g.*, superoxide; $^{\bullet}O^{2-}$).[88–92] These ROS are formed during the normal metabolism of oxygen.[93] Nevertheless, uncertainties remain about their mechanism of toxic action, which is supposed to be exerted mainly through oxidative stress induced by ROS generation, disruption of cell wall and membrane, disruption of mitochondria, enzymatic inhibition protein deactivation, DNA damage or changes in gene expression as well as bacteria wall disruption.[54,94]

Various researches reported that the anti-bacterial activity of CuO NPs is generally attributed to both the released Cu^{2+} ions and the particles CuO themselves.[95,96] The interaction between CuO NPs and biofilm can be considered as a stage process: transfer of NPs in the vicinity of the biofilm, attachment to the biofilm surface, migration in biofilms and biofilm disruption (Fig. 12(a)).

Metal oxide NPs and their ions (*e.g.*, copper, zinc and iron…) can produce free radicals, resulting in induction of oxidative stress. Bacterial contact killing by CuO NPs is preceded by a sequence of specific actions: cell membrane damage, copper influx into the cells, oxidative damage and DNA damage.[54,97] The targeting of DNA by copper leads to rapid DNA fragmentation, resulting in bacterial death,[98] as presented in Fig. 12(b).

Moreover, the addition of 3d transition metal ions as a doping (*e.g.*, Fe; Zn; Co; …) to the metal oxides (MO) lattice results in the increasing of structural defects, which, in turn, enhance their

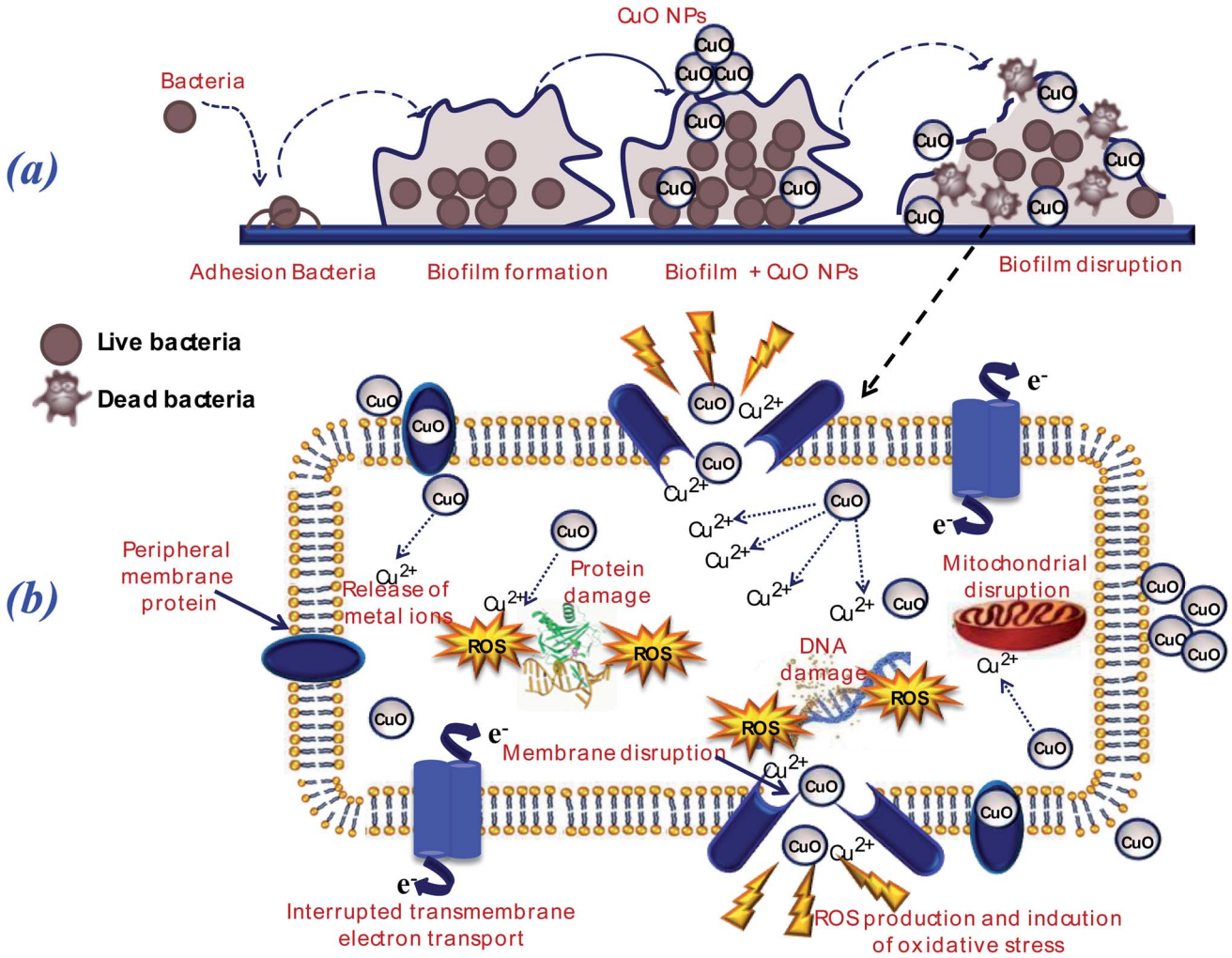

Fig. 12 (a) Illustration of the inhibition of biofilm formation on surfaces coated by CuO NPs. Metal ions (Cu^{2+}) or CuO NPs penetrate the bacteria, the dual functions of nanopowders in killing bacteria and inhibiting biofilm result in biofilm disruption. (b). The mechanism (intra-bacteria) includes cell membrane disruption, disruption of electron transport chains, ROS production, release of metal ions, damage of DNA contents, disruption of mitochondria and protein synthesis.

antibacterial activity due to more ROS generation.[99] Nevertheless, the detailed mechanisms of metal oxide NPs toxicity against various bacteria still not completely understood.

4. Conclusions

In this work, undoped and TM-doped CuO NPs have been successfully synthesized *via* co-precipitation method. The synthesized NPs were characterized by XRD, FT-IR, SEM, EDX and XPS techniques. The X-ray diffraction and EDS analysis confirmed the pure single-phase formation of CuO for all samples. The crystalline size was estimated *via* Debye–Scherrer's law, to be dependent on TM-doping element. The XPS measurements highlight the effective doping, in addition to showing a concentration gradient, with either depletion or an enrichment of the surface in doping element. A difference in morphology of M-doped CuO NPs was also showed by SEM analysis. All these disparities in properties influence the interaction between NPs and the surrounding media.

Besides, all the synthesized samples showed significant anti-adhesive activity against *S. epidermidis S61* biofilms. At high concentrations, CuO:Fe and CuO:Ni exhibit significant improvement over undoped CuO. In contrast, low concentration of CuO:Mn NPs exhibited the strongest anti-adhesive activity. In summary, our results suggest that the synthesized powders can be used as a promising anti-adhesive agent in the biomedical treatment.

In the other hand, it is well known that the mechanisms of oxide NP's toxicity against biofilm bacteria are very complicated and depend on several factors such as composition, surface modification, intrinsic properties (average size, surface area, …), and the bacterial species (Gram-positive or Gram-negative bacteria). Nevertheless, a simplified mechanism is proposed in this paper.

Finally, the obtained results are promising, and pave the way for the synthesis of effective nanopowders to reduce or even eliminate the dangerous effects of biofilms formed by bacteria, and which can find potential applications in the medical field.

Conflicts of interest

There are no conflicts to declare.

Acknowledgements

Authors gratefully thank the financial support of the Tunisian Ministry of Higher Education And Scientific Research, and Campus France, within program (PHC Utique project No 17G1143). Mr P. Decorse (experimental officer) is acknowledged for technical assistance with XPS measurements.

References

1 P. Post, N. Jidenko, A. P. Weber and J.-P. Borra, Post-plasma SiOx coatings of metal and metal oxide nanoparticles for enhanced thermal stability and tunable photoactivity applications, *Nanomaterials*, 2016, **6**, 91.

2 M. S. Dukhinova, A. Prilepskii, A. A. Shtil and V. V. Vinogradov, Metal oxide nanoparticles in therapeutic regulation of macrophage functions, *Nanomaterials*, 2019, **9**, 1631.

3 Y. Abo-zeid and G. R. Williams, The potential anti-infective applications of metal oxide nanoparticles: a systematic review, *Wiley Interdiscip. Rev.: Nanomed. Nanobiotechnol.*, 2020, **12**, e1592.

4 B. D. Harishchandra, *et al.*, Copper nanoparticles: a review on synthesis, characterization and applications, *Asian Pac. J. Cancer Biol.*, 2020, **5**, 201–210.

5 A. Waris, *et al.*, A comprehensive review of green synthesis of copper oxide nanoparticles and their diverse biomedical applications, *Inorg. Chem. Commun.*, 2021, **123**, 108369.

6 H. N. Cuong, *et al.*, New frontiers in the plant extract mediated biosynthesis of copper oxide (CuO) nanoparticles and their potential applications: a review, *Environ. Res.*, 2022, **203**, 111858.

7 Z. Chen, *et al.*, Ultrafine CuO nanoparticles decorated activated tube-like carbon as advanced anode for lithium-ion batteries, *Electrochim. Acta*, 2019, **296**, 206–213.

8 H. Siddiqui, M. R. Parra, P. Pandey, M. Qureshi and F. Z. Haque, Utility of copper oxide nanoparticles (CuO-NPs) as efficient electron donor material in bulk-heterojunction solar cells with enhanced power conversion efficiency, *J. Sci.: Adv. Mater. Devices*, 2020, **5**, 104–110.

9 S. Rajkumar, *et al.*, One-Pot Green Recovery of Copper Oxide nanoparticles from Discarded Printed Circuit Boards for electrode material in Supercapacitor Application, *Resour., Conserv. Recycl.*, 2022, **180**, 106180.

10 F. Peng, *et al.*, Studies on sensing properties and mechanism of CuO nanoparticles to H_2S gas, *Nanomaterials*, 2020, **10**, 774.

11 M. Chauhan, *et al.*, Proficient photocatalytic and sonocatalytic degradation of organic pollutants using CuO nanoparticles, *J. Nanomater.*, 2020, **2020**, 6123178.

12 K. Pakzad, H. Alinezhad and M. Nasrollahzadeh, Green synthesis of Ni@Fe_3O_4 and CuO nanoparticles using Euphorbia maculata extract as photocatalysts for the degradation of organic pollutants under UV-irradiation, *Ceram. Int.*, 2019, **45**, 17173–17182.

13 D. Manyasree, K. M. Peddi and R. Ravikumar, CuO nanoparticles: synthesis, characterization and their bactericidal efficacy, *Int. J. Appl. Pharm.*, 2017, 71–74.

14 T. Cherian, *et al.*, Cymbopogon citratus functionalized green synthesis of CuO-nanoparticles: novel prospects as antibacterial and antibiofilm agents, *Biomolecules*, 2020, **10**, 169.

15 V. Gnanavel, V. Palanichamy and S. M. Roopan, Biosynthesis and characterization of copper oxide nanoparticles and its anticancer activity on human colon cancer cell lines (HCT-116), *J. Photochem. Photobiol., B*, 2017, **171**, 133–138.

16 P. Bhavyasree and T. Xavier, Green synthesised copper and copper oxide based nanomaterials using plant extracts and their application in antimicrobial activity, *Curr. Res. Green Sustainable Chem.*, 2022, **5**, 100249.

17 H. Ahmad, *et al.*, Enhanced biosynthesis synthesis of copper oxide nanoparticles (CuO-NPs) for their antifungal activity toxicity against major phyto-pathogens of apple orchards, *Pharm. Res.*, 2020, **37**, 1–12.

18 S. Ohrt-Nissen, *et al.*, Bacterial biofilms: a possible mechanism for chronic infection in patients with lumbar disc herniation – a prospective proof-of-concept study using fluorescence in situ hybridization, *Apmis*, 2018, **126**, 440–447.

19 T. Bjarnsholt, *et al.*, The impact of mental models on the treatment and research of chronic infections due to biofilms, *Apmis*, 2021, **129**, 598–606.

20 M. A. Rather, *et al.*, Microbial biofilm: a matter of grave concern for human health and food industry, *J. Basic Microbiol.*, 2021, **61**, 380–395.

21 K. McNamara and S. A. Tofail, Nanoparticles in biomedical applications, *Adv. Phys.: X*, 2017, **2**, 54–88.

22 B. Bai, *et al.*, Biosynthesized copper oxide nanoparticles (CuO NPs) enhances the anti-biofilm efficacy against *K. pneumoniae* and *S. aureus*, *J. King Saud Univ., Sci.*, 2022, 102120.

23 P. S. Murthy, V. Pandiyan and A. Das, *Emerging Nanomaterials for Advanced Technologies*, Springer, 2022, pp. 163–209.

24 S. Sathiyavimal, *et al.*, Biogenesis of copper oxide nanoparticles (CuONPs) using Sida acuta and their incorporation over cotton fabrics to prevent the pathogenicity of Gram negative and Gram positive bacteria, *J. Photochem. Photobiol., B*, 2018, **188**, 126–134.

25 M. Eshed, J. Lellouche, A. Gedanken and E. Banin, A Zn-doped CuO nanocomposite shows enhanced antibiofilm and antibacterial activities against streptococcus mutans compared to nanosized CuO, *Adv. Funct. Mater.*, 2014, **24**, 1382–1390.

26 A. Pramothkumar, N. Senthilkumar, K. M. G. Malar, M. Meena and I. V. Potheher, A comparative analysis on the dye degradation efficiency of pure, Co, Ni and Mn-doped CuO nanoparticles, *J. Mater. Sci.: Mater. Electron.*, 2019, **30**, 19043–19059.

27 K. Deepa and T. Venkatesha, Synthesis and Generation of CuO and Mn Doped CuO Composites and its Corrosion Behaviour, *Mater. Today: Proc.*, 2017, **4**, 12045–12053.
28 V. Ponnarasan and A. Krishnan, Synthesis, Structural and Optical Properties of Cobalt Doped CuO Nanoparticles, *Int. J. Nanosci.*, 2017, **16**, 1650031.
29 Z. Pezeshki-Nejad, S. Alikhanzadeh-Arani and M. A. Kashi, Magnetic phase tuning of diluted Fe-doped CuO nanoparticles through annealing temperature as characterized by first-order reversal curve analysis, *J. Magn. Magn. Mater.*, 2019, **482**, 301–311.
30 S. Al-Amri, *et al.*, Ni doped CuO nanoparticles: structural and optical characterizations, *Curr. Nanosci.*, 2015, **11**, 191–197.
31 R. Yathisha, *et al.*, Study on the effect of Zn^{2+} doping on optical and electrical properties of CuO nanoparticles, *Phys. E*, 2019, **108**, 257–268.
32 F. Erci, R. Cakir-Koc, M. Yontem and E. Torlak, Synthesis of biologically active copper oxide nanoparticles as promising novel antibacterial-antibiofilm agents, *Prep. Biochem. Biotechnol.*, 2020, **50**, 538–548.
33 A. Pugazhendhi, S. S. Kumar, M. Manikandan and M. Saravanan, Photocatalytic properties and antimicrobial efficacy of Fe doped CuO nanoparticles against the pathogenic bacteria and fungi, *Microb. Pathog.*, 2018, **122**, 84–89.
34 M. Loza-Correa, B. Yousuf and S. Ramirez-Arcos, Staphylococcus epidermidis undergoes global changes in gene expression during biofilm maturation in platelet concentrates, *Transfusion*, 2021, **61**, 2146–2158.
35 M. Otto, Staphylococcal biofilms, *Bact. Biofilms*, 2008, 207–228.
36 M. Sabaté Brescó, *et al.*, Pathogenic mechanisms and host interactions in Staphylococcus epidermidis device-related infection, *Front. Microbiol.*, 2017, **8**, 1401.
37 H. Büttner, D. Mack and H. Rohde, Structural basis of Staphylococcus epidermidis biofilm formation: mechanisms and molecular interactions, *Front. Cell. Infect. Microbiol.*, 2015, **5**, 14.
38 W. M. Mohammed, T. H. Mubark and R. M. Al-Haddad, Effect of CuO nanoparticles on antimicrobial activity prepared by sol-gel method, *Int. J. Appl. Eng. Res. Dev.*, 2018, **13**, 10559–10562.
39 I. Z. Luna and B. A. E. Commission, Preparation and characterization of copper oxide nanoparticles synthesized via chemical precipitation method, *Open Access Library Journal*, 2015, **2**, 1.
40 L. B. Chandrasekar, R. Chandramohan, M. Karunakaran and R. Vijayalakshmi, Synthesis and characterization of copper oxide and zinc oxide nanomaterials, *Nat. Sci. Mater.*, 2016, **1**, 18–22.
41 M. Ponnar, C. Thangamani, P. Monisha, S. Gomathi and K. Pushpanathan, Influence of Ce doping on CuO nanoparticles synthesized by microwave irradiation method, *Appl. Surf. Sci.*, 2018, **449**, 132–143.
42 K. Khashan, M. Jabir and F. Abdulameer, *J. Phys.: Conf. Ser.*, 2018, 012100.
43 G. K. Weldegebrieal, Photocatalytic and antibacterial activityof CuO nanoparticles biosynthesized using Verbascum thapsus leaves extract, *Optik*, 2020, **204**, 164230.
44 A. I. El-Batal, G. S. El-Sayyad, F. M. Mosallam and R. M. Fathy, Penicillium chrysogenum-mediated mycogenic synthesis of copper oxide nanoparticles using gamma rays for in vitro antimicrobial activity against some plant pathogens, *J. Cluster Sci.*, 2020, **31**, 79–90.
45 T. G. Vladkova, A. D. Staneva and D. N. Gospodinova, Surface engineered biomaterials and ureteral stents inhibiting biofilm formation and encrustation, *Surf. Coat. Technol.*, 2020, **404**, 126424.
46 M. Jardak, *et al.*, Evaluation of biofilm-forming ability of bacterial strains isolated from the roof of an old house, *J. Gen. Appl. Microbiol.*, 2017, **63**(3), 186–194.
47 A. Nostro, *et al.*, Effects of oregano, carvacrol and thymol on Staphylococcus aureus and Staphylococcus epidermidis biofilms, *J. Med. Microbiol.*, 2007, **56**, 519–523.
48 N. Calos, J. Forrester and G. Schaffer, A crystallographic contribution to the mechanism of a mechanically induced solid state reaction, *J. Solid State Chem.*, 1996, **122**, 273–280.
49 S. Singhal, J. Kaur, T. Namgyal and R. Sharma, Cu-doped ZnO nanoparticles: synthesis, structural and electrical properties, *Phys. B*, 2012, **407**, 1223–1226.
50 R. D. Shannon, Revised effective ionic radii and systematic studies of interatomic distances in halides and chalcogenides, *Acta Crystallogr., Sect. A: Cryst. Phys., Diffr., Theor. Gen. Crystallogr.*, 1976, **32**, 751–767.
51 H. Kafashan, X-ray diffraction line profile analysis of undoped and Se-doped SnS thin films using Scherrer's, Williamson–Hall and size–strain plot methods, *J. Electron. Mater.*, 2019, **48**, 1294–1309.
52 P. Scherrer, *Kolloidchemie Ein Lehrbuch*, Springer, 1912, pp. 387–409.
53 J. I. Langford and A. Wilson, Scherrer after sixty years: a survey and some new results in the determination of crystallite size, *J. Appl. Crystallogr.*, 1978, **11**, 102–113.
54 K. Ali, *et al.*, Comparative in situ ROS mediated killing of bacteria with bulk analogue, Eucalyptus leaf extract (ELE)-capped and bare surface copper oxide nanoparticles, *Mater. Sci. Eng., C*, 2019, **100**, 747–758.
55 K. Rogers and P. Daniels, An X-ray diffraction study of the effects of heat treatment on bone mineral microstructure, *Biomaterials*, 2002, **23**, 2577–2585.
56 T. Srinivasulu, K. Saritha and K. R. Reddy, Synthesis and characterization of Fe-doped ZnO thin films deposited by chemical spray pyrolysis, *Mod. Electron. Mater.*, 2017, **3**, 76–85.
57 J. Gubicza, J. Szépvölgyi, I. Mohai, L. Zsoldos and T. Ungár, Particle size distribution and dislocation density determined by high resolution X-ray diffraction in nanocrystalline silicon nitride powders, *Mater. Sci. Eng., A*, 2000, **280**, 263–269.
58 B. K. Ku and P. Kulkarni, Comparison of diffusion charging and mobility-based methods for measurement of aerosol agglomerate surface area, *J. Aerosol Sci.*, 2012, **47**, 100–110.

59 J. Chen, Y. Li, Y. Wang, J. Yun and D. Cao, Preparation and characterization of zinc sulfide nanoparticles under high-gravity environment, *Mater. Res. Bull.*, 2004, **39**, 185–194.
60 S. Qayyum and A. U. Khan, Nanoparticles *vs.* biofilms: a battle against another paradigm of antibiotic resistance, *MedChemComm*, 2016, **7**, 1479–1498.
61 A. Jain, S. Ranjan, N. Dasgupta and C. Ramalingam, Nanomaterials in food and agriculture: an overview on their safety concerns and regulatory issues, *Crit. Rev. Food Sci. Nutr.*, 2018, **58**, 297–317.
62 R. Sahay, *et al.*, Synthesis and characterization of CuO nanofibers, and investigation for its suitability as blocking layer in ZnO NPs based dye sensitized solar cell and as photocatalyst in organic dye degradation, *J. Solid State Chem.*, 2012, **186**, 261–267.
63 O. P. Keabadile, A. O. Aremu, S. E. Elugoke and O. E. Fayemi, Green and Traditional Synthesis of Copper Oxide Nanoparticles—Comparative Study, *Nanomaterials*, 2020, **10**, 2502.
64 P. V. Kumar, U. Shameem, P. Kollu, R. Kalyani and S. Pammi, Green synthesis of copper oxide nanoparticles using Aloe vera leaf extract and its antibacterial activity against fish bacterial pathogens, *BioNanoScience*, 2015, **5**, 135–139.
65 G. Kliche and Z. Popovic, Far-infrared spectroscopic investigations on CuO, *Phys. Rev. B: Condens. Matter Mater. Phys.*, 1990, **42**, 10060.
66 K. Nakamoto, *Infrared and Raman spectra of inorganic and coordination compounds, part B: applications in coordination, organometallic, and bioinorganic chemistry*, John Wiley & Sons, 2009.
67 A. Rahnama and M. Gharagozlou, Preparation and properties of semiconductor CuO nanoparticles via a simple precipitation method at different reaction temperatures, *Opt. Quant. Electron.*, 2012, **44**, 313–322.
68 P. K. Raul, *et al.*, CuO nanorods: a potential and efficient adsorbent in water purification, *RSC Adv.*, 2014, **4**, 40580–40587.
69 L. Zheng and X. Liu, Solution-phase synthesis of CuO hierarchical nanosheets at near-neutral pH and near-room temperature, *Mater. Lett.*, 2007, **61**, 2222–2226.
70 D. Dubal, D. Dhawale, R. Salunkhe, V. Jamdade and C. Lokhande, Fabrication of copper oxide multilayer nanosheets for supercapacitor application, *J. Alloys Compd.*, 2010, **492**, 26–30.
71 N. A. Bakr, T. A. Al-Dhahir and S. B. Mohammad, Growth of copper sulfate pentahydrate single crystals by slow evaporation technique, *J. Adv. Phys.*, 2017, **13**, 4651–4656.
72 E. Darezereshki and F. Bakhtiari, A novel technique to synthesis of tenorite (CuO) nanoparticles from low concentration $CuSO_4$ solution, *J. Min. Metall., Sect. B*, 2011, **47**, 73–78.
73 M. Ohnishi, I. Kusachi, S. Kobayashi and J. Yamakawa, Mineral chemistry of schulenbergite and its Zn-dominant analogue from the Hirao mine, Osaka, Japan, *J. Mineral. Petrol. Sci.*, 2007, **102**, 233–239.
74 A. Brisdon, Infrared and Raman Spectra of Inorganic and Coordination Compounds, Part B, Applications in Coordination, *Organometallic, and Bioinorganic Chemistry*, 6th edn, Wiley, 2009, p. 424. ISBN 978-0-471-744931, DOI: 10.1002/aoc.1655.
75 S. Meshram, P. Adhyapak, U. Mulik and D. Amalnerkar, Facile synthesis of CuO nanomorphs and their morphology dependent sunlight driven photocatalytic properties, *Chem. Eng. J.*, 2012, **204**, 158–168.
76 J. A. Bearden and A. Burr, Reevaluation of X-ray atomic energy levels, *Rev. Mod. Phys.*, 1967, **39**, 125.
77 M. C. Biesinger, Advanced analysis of copper X-ray photoelectron spectra, *Surf. Interface Anal.*, 2017, **49**, 1325–1334.
78 Database, *NIST Standard Reference Database Number 20*, National Institute of Standards and Technology, Gaithersburg MD, 2000, p. 20899.
79 M. Jo and A. Tanaka, Auger electron peaks of Cu in XPS, *Appl. Surf. Sci.*, 1996, **100**, 11–14.
80 B. J. Tan, K. J. Klabunde and P. M. Sherwood, X-ray photoelectron spectroscopy studies of solvated metal atom dispersed catalysts. Monometallic iron and bimetallic iron-cobalt particles on alumina, *Chem. Mater.*, 1990, **2**, 186–191.
81 S. Liu, *et al.*, In situ construction of hybrid Co (OH) 2 nanowires for promoting long-term water splitting, *Appl. Catal., B*, 2021, **292**, 120063.
82 K. M. Cole, D. W. Kirk and S. J. Thorpe, $Co(OH)_2$ powder characterized by X-ray photoelectron spectroscopy (XPS) and ultraviolet photoelectron spectroscopy (UPS), *Surf. Sci. Spectra*, 2020, **27**, 024013.
83 K. Li and D. Xue, Estimation of electronegativity values of elements in different valence states, *J. Phys. Chem. A*, 2006, **110**, 11332–11337.
84 L. Wang, C. Hu and L. Shao, The antimicrobial activity of nanoparticles: present situation and prospects for the future, *Int. J. Nanomed.*, 2017, **12**, 1227.
85 S. Fulaz, S. Vitale, L. Quinn and E. Casey, Nanoparticle–biofilm interactions: the role of the EPS matrix, *Trends Microbiol.*, 2019, **27**, 915–926.
86 B. Maroua, *et al.*, *Oxidative Stress Induced By The Metallic Oxide The Copper Oxide (CuO-NPs) On Terrestrial Snail Helix Aspersa*, 2021.
87 E. I. Hassanen, *et al.*, Ameliorative effect of ZnO-NPs against bioaggregation and systemic toxicity of lead oxide in some organs of albino rats, *Environ. Sci. Pollut. Res.*, 2021, 1–13.
88 X. Zhang, F. Tian, M. Gao, W. Yang and Y. Yu, L-Cysteine capped Mo2C/Zn0. 67Cd0. 33S heterojunction with intimate covalent bonds enables efficient and stable H2-Releasing photocatalysis, *Chem. Eng. J.*, 2022, **428**, 132628.
89 X. Zhang, *et al.*, Building P-doped MoS2/g-C3N4 layered heterojunction with a dual-internal electric field for efficient photocatalytic sterilization, *Chem. Eng. J.*, 2022, **429**, 132588.
90 S. Bao, Y. Wang, Z. Wei, W. Yang and Y. Yu, Highly efficient recovery of heavy rare earth elements by using an amino-functionalized magnetic graphene oxide with acid and base resistance, *J. Hazard. Mater.*, 2022, **424**, 127370.

91 X. Zhang, *et al.*, Room-temperature solid phase surface engineering of BiOI sheets stacking g-C3N4 boosts photocatalytic reduction of Cr (VI), *Green Energy Environ.*, 2020, **7**(1), 66–74.

92 S. Geng, *et al.*, Activating interfacial S sites of MoS_2 boosts hydrogen evolution electrocatalysis, *Nano Res.*, 2022, **15**, 1809–1816.

93 C. A. Juan, J. M. Pérez de la Lastra, F. J. Plou and E. Pérez-Lebeña, The Chemistry of Reactive Oxygen Species (ROS) Revisited: Outlining Their Role in Biological Macromolecules (DNA, Lipids and Proteins) and Induced Pathologies, *Int. J. Mol. Sci.*, 2021, **22**, 4642.

94 Y. N. Slavin, J. Asnis, U. O. Häfeli and H. Bach, Metal nanoparticles: understanding the mechanisms behind antibacterial activity, *J. Nanobiotechnol.*, 2017, **15**, 1–20.

95 C. Angelé-Martínez, *et al.*, Polyphenol effects on CuO-nanoparticle-mediated DNA damage, reactive oxygen species generation, and fibroblast cell death, *Toxicol. in Vitro*, 2022, **78**, 105252.

96 D. Vinu, *et al.*, Biogenic zinc oxide, copper oxide and selenium nanoparticles: preparation, characterization and their anti-bacterial activity against Vibrio parahaemolyticus, *J. Nanostruct. Chem.*, 2021, **11**, 271–286.

97 B. M. Strauch, R. K. Niemand, N. L. Winkelbeiner and A. Hartwig, Comparison between micro-and nanosized copper oxide and water soluble copper chloride: interrelationship between intracellular copper concentrations, oxidative stress and DNA damage response in human lung cells, *Part. Fibre Toxicol.*, 2017, **14**, 1–17.

98 H. Yang, C. Liu, D. Yang, H. Zhang and Z. Xi, Comparative study of cytotoxicity, oxidative stress and genotoxicity induced by four typical nanomaterials: the role of particle size, shape and composition, *J. Appl. Toxicol.*, 2009, **29**, 69–78.

99 D. Smyth, The effects of dopants on the properties of metal oxides, *Solid State Ionics*, 2000, **129**, 5–12.